LANGMUIR

pubs.acs.org/Langmuir Article

Membrane Remodeling by DNA Origami Nanorods: Experiments Exploring the Parameter Space for Vesicle Remodeling

Sarah E. Zuraw-Weston, Mahsa Siavashpouri, Maria E. Moustaka, Thomas Gerling, Hendrik Dietz, Seth Fraden, Alexander E. Ribbe, and Anthony D. Dinsmore*



Cite This: Langmuir 2021, 37, 6219-6231



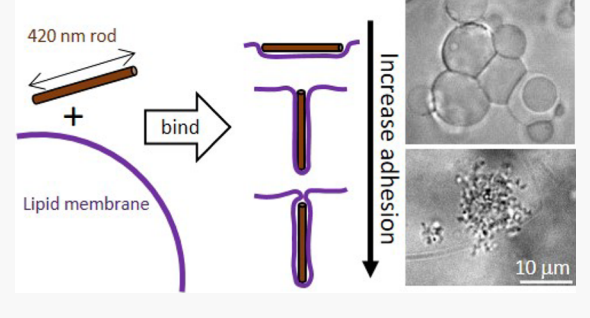
ACCESS

III Metrics & More

Article Recommendations

Supporting Information

ABSTRACT: Inspired by the ability of cell membranes to alter their shape in response to bound particles, we report an experimental study of long, slender nanorods binding to lipid bilayer vesicles and altering the membrane shape. Our work illuminates the role of particle concentration, adhesion strength, and membrane tension in determining the membrane morphology. We combined giant unilamellar vesicles with oppositely charged nanorods, carefully tuning the adhesion strength, membrane tension, and particle concentration. With increasing adhesion strength, the primary behaviors observed were membrane deformation, vesicle—vesicle adhesion, and vesicle rupture. These behaviors were observed in well-defined regions in the parameter space with sharp transitions between



them. We observed the deformation of the membrane resulting in tubulation, textured surfaces, and small and large lipid—particle aggregates. These responses are robust and repeatable and provide a new physical understanding of the dependence on the shape, binding affinity, and particle concentration in membrane remodeling. The design principles derived from these experiments may lead to new bioinspired membrane-based materials.

■ INTRODUCTION

Lipid bilayer membranes are remarkable materials with a wide range of important applications due to their flexibility, in-plane fluidity, impermeability to solutes, and ability to host membrane-associated macromolecules or particles. 1,2 Live cells offer many inspiring examples, in which the membrane shape and function are remodeled from the simple spherical shape of a vesicle: the bicontinuous structure of the endoplasmic reticulum,³ plasma-membrane protrusions leading to cell motility,^{4–7} and wrapping and uptake of filamentous Ebola virus. 8-12 There has been great progress in applying synthetic lipid bilayers for encapsulation and delivery 13 and for biosensors that monitor food toxicants and environmental pollutants.¹⁴ Nonetheless, there are still key unique properties of lipid membranes and inspirations from biology that have yet to be realized. For example, controlling particle binding, membrane adhesion, and membrane shape would allow for triggerable membrane remodeling and new, responsive membrane-based materials.

Realizing these examples requires that we first understand the interactions of membranes with particles of various sizes and shapes and then develop the control parameters that determine the response. Theory, simulations, and experiments showed that when a rigid particle binds weakly, it deforms the membrane. The deformation comes from adhesion energy per area, ω , which competes with the membrane's bending stiffness κ , tension, $^{15-20}$ or osmotic pressure. When many particles are

present, the deformed membrane induces in-plane particle interactions and assembly, which can amplify the membrane response and cause large-scale remodeling. $^{4,9,10,18,19,22-24}$ With sufficiently strong adhesion, the particle is fully wrapped by the membrane. $^{9,15,25-27}$ For spherical particles of radius a having short-ranged attraction, this single-particle wrapping occurs when $\omega a^2/\kappa$ exceeds a threshold of the order of 1, if $\tau a^2/\kappa \ll 1$ (generally true for nanoparticles). Recently, a combined experimental and simulation study showed that spherical nanoparticles binding to vesicles with controlled adhesion strength show a sharp and tunable crossover from weak deformation (leading to adhesion among vesicles) to wrapping of particles (leading by a sequence of stages to vesicle destruction). 26

The results obtained for spherical particles led us to ask whether a less symmetric particle shape—long slender rods—would induce different behavior because the energy cost for bending the membrane and wrapping particles changes. Cells offer the inspiring example of cylindrical membrane protrusions (filopodia) that are in part driven by bundled actin filaments.⁴

Received: February 10, 2021 Revised: April 26, 2021 Published: May 13, 2021





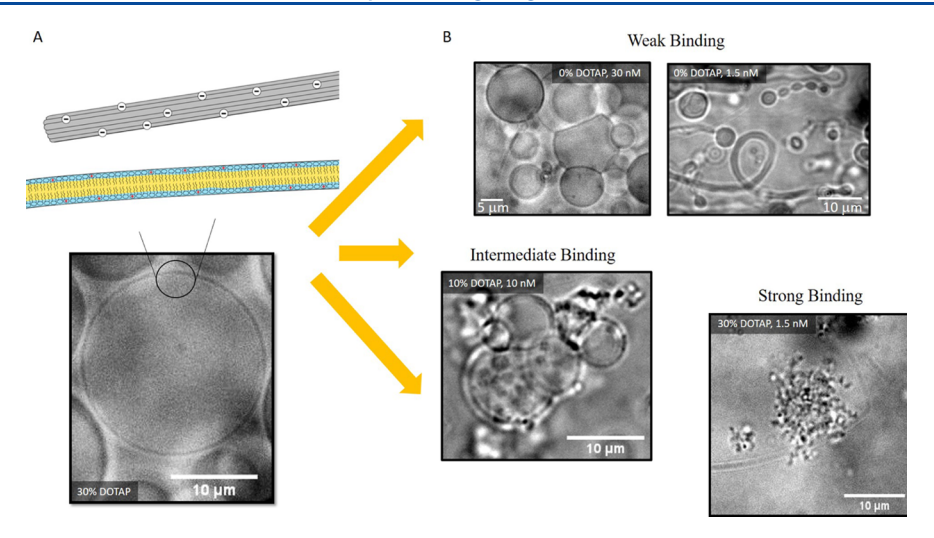


Figure 1. (A) Schematic overview of GUVs with tunable charge density controlled by the amount of cationic lipid present in the membrane interacting with anionic DNA origami nanorods. The micrograph image shows a GUV composed of 70% DOPC and 30% DOTAP prior to the addition of nanorods. (B) Microscopy images of GUVs combined with nanorods with increasing amounts of DOTAP associated with weak, intermediate, and strong binding of particles to the membrane resulting in deformation, adhesion, and/or rupture of the vesicles.

Experiments with flexible fd virus particles binding to membranes showed tip-to-tip aggregation or rod collapse with the strongest binding. 28,29 In recent experiments with more rigid rods made by DNA origami, the particle shape determined whether the vesicle retained its approximately spherical shape (observed with straight rods) or deformed by tubules or dimples (with curved rods). 18 In the latter experiments, the rodmembrane interaction was strong enough for adhesion but not enough for wrapping. 18,28,30,31 In cells (not necessarily the same as vesicles), long ellipsoids or rods were phagocytosed more rapidly and efficiently than spheres, ^{32,33} while other experiments found less phagocytosis but greater exocytosis. 11 Presumably, these cellular uptake studies were done in the regime of higher ω leading to particle wrapping, but this is not always known. Simulations have shown that rigid rods have more than two wrapping configurations (unlike spheres), separated by discontinuous crossovers determined by $\omega a^2/\kappa$ and the rod's aspect ratio. 25,34 The questions we seek to answer by experiments are the following: Is there a crossover in collective behavior between weak binding and strong binding? How do the uniaxial particle shape and presence of two wrapping transitions change the particle-membrane interactions and the morphol-

Here, we report the results of a well-defined system of lipid membrane and rod-shaped nanoparticles, wherein we tune the interaction strength ω , membrane tension τ , and particle concentration c_{rod} . For particles, we used anionic DNA origami nanorods that are 420 nm long and 5 nm in diameter. These particles were selected for their size monodispersity, uniform charge density, hydrophilicity, and stability in suspension. We used giant unilamellar vesicles (GUVs), $10-100 \mu m$ in diameter, composed of a zwitterionic lipid (DOPC) and a cationic lipid (DOTAP) (a mixture used previously 26,28). The rods were attracted to the membrane by electrostatic doublelayer forces. 26 The interaction strength ω was tuned by the fraction of the DOTAP in the membrane, x. We studied the dynamics and steady state of the system using bright-field, darkfield, and fluorescence optical microscopy, and we used cryogenic electron microscopy (cryo-EM) to image the rods at the nanometer scale. We found that with low x and low c_{rod} particles deformed the membrane into tubules and other shapes.

With low x and high c_{rod} , we observed vesicle—vesicle adhesion and a vesicle-based gel. With higher x (higher ω), we observed a crossover into vesicle rupture simultaneously with vesiclevesicle adhesion. At still higher x, we found a second crossover to vesicle rupture without vesicle—vesicle adhesion. The process of vesicle destruction was complex, involving aggregates, tubules, sudden drops in the vesicle's radius, and shrinking of the vesicle until final rupture. The sequence of events was repeatable over a large portion of the parameter space. We also found that the second crossover shifted toward smaller x in vesicles with excess area. Cryo-EM provided the first evidence of membranemediated interactions among rods, leading to the parallel alignment of membrane-bound rods in some regions of the membrane and aster-like rod formations and a new deformation mode in other regions. We present these results in a state diagram and conclude that the two crossovers arise from the two separate wrapping transitions at the single-rod scale. Compared to our earlier study of spherical particles, the rods exhibit many of the same behaviors such as the formation of a bulk vesicle gel and vesicle destruction. However, rods order on the membrane and also induce an additional intermediate state of vesicle adhesion followed by rupture (Figure 1).

The ability to tune morphology opens the door to smart, responsive, and membrane-based materials such as cargo-carrying vesicle gels that rupture when exposed to external stimuli or exhibit controlled release over extended periods of time. Our results provide a detailed presentation of the state space defined by ω , κ , τ , and $c_{\rm rod}$ and provide new insights into membrane-mediated forces among bound rods such as bundled actin or filamentous virus. The variety of phenomena and the controlled parameters make this system ideal for comparison with theory and simulation.

■ EXPERIMENTAL SECTION

GUVs were formed using electroformation.³⁶ We used a zwitterionic mono-unsaturated 1,2-dioleoyl-sn-glycero-3-phosphocholine (18:1 DOPC; Avanti Polar Lipids). We also used cationic 1,2-dioleoyl-3-trimethylammonium-propane (18:1 DOTAP; Avanti Polar Lipids) to tune the charge density, as it has the same fatty acid tail as DOPC (to suppress demixing). We were careful to keep all tools and surfaces clean at every step and we found good yield from electroformation for all

DOTAP mole fractions. In order to visualize the membrane using confocal microscopy, we added to some samples a small amount of headgroup-labeled lipid 1,2-dioleoyl-sn-glycero-3-phosphoethanol-amine-N-(lissamine rhodamine B sulfonyl) (ammonium salt) (Rh-DOPE; Avanti Polar Lipids). Care was also taken to control the osmolarity of the vesicles in all cases. Vesicles referred to as balanced were formed in a sucrose solution at 175 mOsm/L and then diluted in an equal volume of glucose solution at 180 mOsm/L. The vesicles were then left overnight to sediment as well as equilibrate. Vesicles referred to as floppy were prepared in the same way initially but were then diluted in a glucose solution at 200 mOsm/L within 5 min of experimental observation. The 10% difference in the interior and exterior osmolarities resulted in floppier vesicles with excess area.

Anionic DNA origami nanorods were formed from six-helix DNA bundles into rods that are 420 nm by 6 nm with a right-handed twist (360°) . For the low ionic strength conditions used in our experiments, the rods had to be further structurally stabilized. To this end, nanorods were specifically designed with strategically placed additional thymidines and then exposed to ultraviolet light, which induces covalent bonds between them. The rods were synthesized and finally stored in a 1 × FOBMg5 buffer composed of 5 mM TRIS, 5 mM NaCL, 1 mM EDTA, and 5 mM MgCl at pH 8. The final concentration of rods was 150 nM. From this stock solution, rods were diluted using the same sucrose and glucose solution used to create and dilute the vesicles. The concentration, $c_{\rm rod}$, is denoted per experiment.

Experiments were conducted in custom flow chambers with microfluidic wells that enabled the real-time visualization of particle membrane interactions. The experiment chambers also allowed for the careful control of the bulk solution (Figure S1). Vesicles were injected into the chambers and then allowed to sediment into PDMS wells at the bottom of the chamber. Once the vesicles had sedimented in a layer that was 1-2 vesicles deep, the bulk fluid of the chamber was rapidly replaced with a solution having the desired $c_{\rm rod}$. Vesicles comprised less than 1% of the sample volume and there was a large excess of rods relative to the number needed to fully coat the membranes. The chamber was mounted on an optical microscope and interactions were observed from beneath. See Supporting Information for more information.

RESULTS

In this section, we describe the phenomenology observed due to the deformation of lipid bilayer membranes by DNA origami nanorods. This section is divided into six subsections. The first provides an overview of the phenomenology and presents a state diagram of our results (Figure 2). The next four describe the four primary behaviors depicted in our state diagram. In the final subsection, we present results from cryogenic transmission electron microscopy (cryo-TEM) in the strong binding regime. In the Discussion section, we present hypotheses for the underlying mechanisms and compare it to previous literature.

Overview of the Phenomenology: Regimes of Deformation, Adhesion, and Rupture. We studied the response of vesicles in situ after the introduction of anionic DNA origami nanorods. The vesicles were captured and confined using microfluidic wells, and the bulk suspension was replaced with a solution with a fixed concentration of nanorod, c_{rod} . In all cases, there was a large excess of rods so that even the complete disruption of all the vesicles would only consume roughly 1% of them for $c_{\text{rod}} = 10$ nM. Increasing c_{rod} effectively increased the rod chemical potential and the diffusive binding rate of nanorods onto the membrane. We also tuned the adhesion energy per area, ω , between the lipid bilayer and the oppositely charged nanorods by increasing the amount of cationic lipid content in the vesicles, *x*. To probe the dependence on membrane tension, τ , or excess area, we examined two populations of vesicles: those that were osmotically balanced (referred to as balanced) and

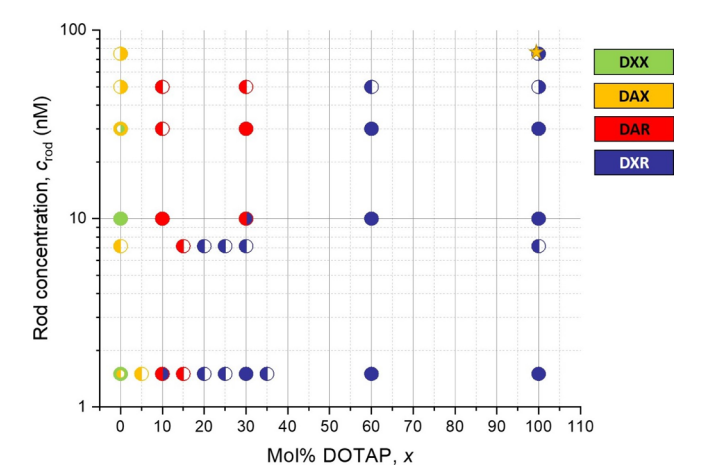


Figure 2. State diagram of the observed interactions of GUVs with DNA origami nanorods. Increasing the DOTAP % is directly correlated with an increase in the adhesion strength between the particles and the membrane. Green circles denote vesicles in the DXX regime (deformation, no adhesion, no rupture). Yellow circles denote vesicles in the DAX regime (deformation, adhesion, no rupture). Red circles denote vesicles in the DAR regime (deformation, adhesion, rupture). Blue circles denote vesicles in the DXR regime (deformation, no adhesion, rupture). Circles filled on the right-hand side denote results for vesicles that are osmotically balanced. Circles filled on the left side denote results for vesicles that are floppy due to exposure to a hypertonic solution. Full circles represent results for both balanced and floppy vesicles. The yellow star at x = 100% and $c_{\rm rod} = 75$ nM represents a sample imaged with a cryogenic electron microscope.

those that were saturated in a hypertonic solution (referred to as floppy). Care was taken to ensure that all solutions had equal osmolarity so that osmotic shock did not play a role in the processes described here. In control experiments without rods, we observed only intact vesicles without adhesion. In the presence of rods, dark-field microscopy provided direct evidence that rods bound to the membrane (Figure S2).

Figure 2 depicts a state diagram for the system, in steady state, as a function of c_{rod} , x, and excess area. In all cases, we observed some combination of three distinct behaviors, and the presence or lack of these behaviors defined four primary regimes in the state diagram. In order, the triplet of primary responses was membrane deformation (D), vesicle-vesicle adhesion (A), and vesicle rupture (R), while an absence of one of these behaviors was noted by (X). Remarkably, the onsets of these behaviors were sharply defined in Figure 2, so that we could define transitions between regimes corresponding to the various behaviors. At low DOTAP concentrations, we observed the DXX and DAX regimes where vesicles deformed in shape and adhered to one another but remained intact after the introduction of rods. At a higher DOTAP concentration, x, we found a crossover to the DAR regime, wherein vesicle rupture and destruction were also observed. With still higher x, we found a second crossover to the destruction of individual vesicles with no adhesion (DXR). For intermediate DOTAP (10-30 mol %), increasing c_{rod} led to a crossover from DXR to DAR, corresponding to the onset of intervesicle adhesion. We also found that increasing the excess area in the vesicles (making them floppy initially) shifted the system toward DXR rather than DAR, and hence tended to favor singe-vesicle destruction. Figures 3, S3 show in greater detail the behaviors observed throughout the state diagram. We now discuss these regimes in detail.

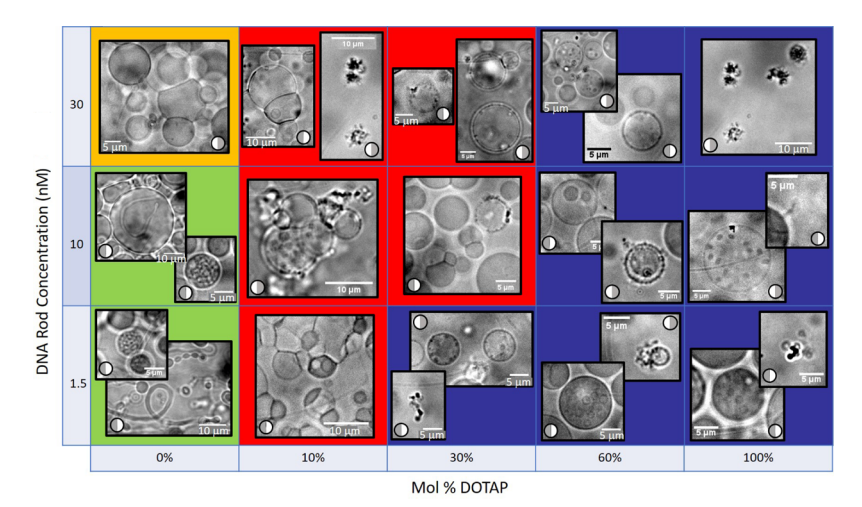


Figure 3. Pictorial representation of the state space with micrograph images, depicting the most commonly observed phenomena in each regime. As in Figure 2, green denotes vesicles in the DXX regime (deformation, no adhesion, no rupture). Yellow denotes vesicles in DAX (deformation, adhesion, no rupture). Red denotes vesicles in DAR (deformation, adhesion, rupture). Blue denotes vesicles in DXR (deformation, no adhesion, rupture). Right-filled semicircles denote results for vesicles that were floppy due to their exposure to a hypertonic solution. Scale bar length is denoted in each micrograph.

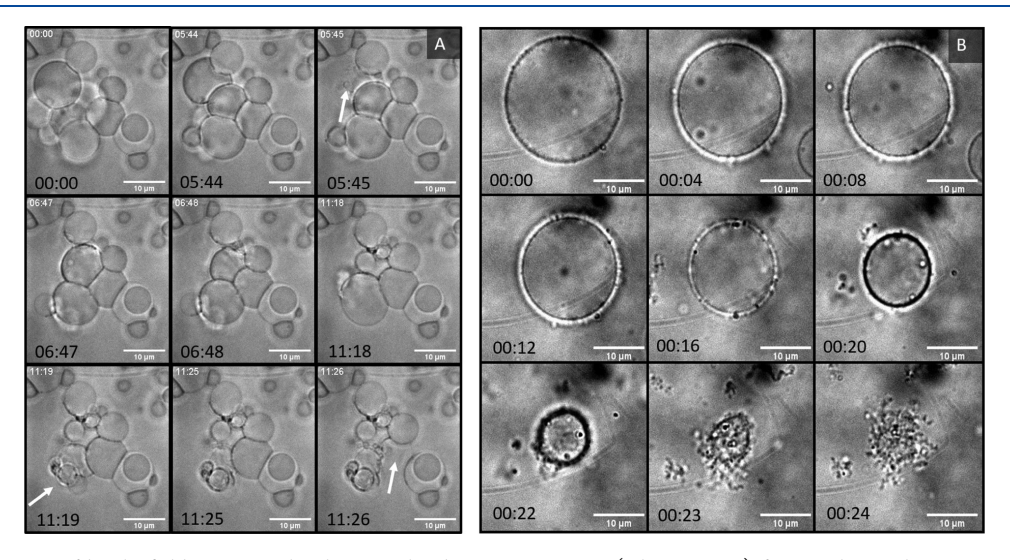


Figure 4. (A) Montage of bright-field micrographs showing the disruption process (white arrows) for vesicles in the DAR regime. The vesicles contained 10 mol % DOTAP and were exposed to DNA origami rods at 1.5 nM concentration. (B) Montage of bright-field micrographs showing the disruption process in the DXR regime. The vesicle contained 30 mol % DOTAP and were exposed to DNA origami rods at 1.5 nM concentration. Scale bars are $10~\mu m$.

DXX Regime: Deformation of Individual Vesicles. For membranes without DOTAP (x = 0) and low c_{rod} , we saw nanorods binding to vesicles, leading to the deformation of the vesicles without vesicle-vesicle adhesion. Particles adhered to the vesicles reconfiguring the membrane into three morphologies: elongated shapes, tubules, or dense textured surfaces on the vesicles (Figure 3, green region). The elongated configuration was observed for the majority of vesicles in this regime. Previously spherical vesicles were elongated into tubular configurations that were sometimes as narrow as only a few μm in diameter. Some vesicles were dramatically elongated while others developed only mild elongation with aspect ratios closer to 2:1, while still others kept their spherical shape. Tubules, defined here as narrow tubular protrusions from roughly spherical vesicles, were also very common for both spherical and elongated vesicles. We observed both internal and external tubules, with external tubules being more common.

These tubules were stable for the duration of the experiment. The third morphology seen in the DXX regime (1 or 2 vesicles out of 100 in a typical field-of-view) was spherical vesicles with highly textured surfaces. Two examples are given in the green DXX portion of Figure 3. The patterned surface was only seen on spherical vesicles and was never accompanied by tubules. The pattern was stiff, barely fluctuating or deforming. The elongated shapes, tubules, and textured surface were observed for both balanced and floppy vesicles without any discernible dependence on excess area, (Supporting Information Video S4).

DAX Regime: Deformation and Vesicle–Vesicle Adhesion. In other samples at low DOTAP, and particularly at higher c_{rod} , we found adhesion between vesicles as well as deformation (DAX). The membranes of neighboring vesicles adhered to one another due to the bound nanorods forming an adhesive bridge. Dark-field microscopy images (Figure S2) show strong light scattering at the adhesion sites between vesicles

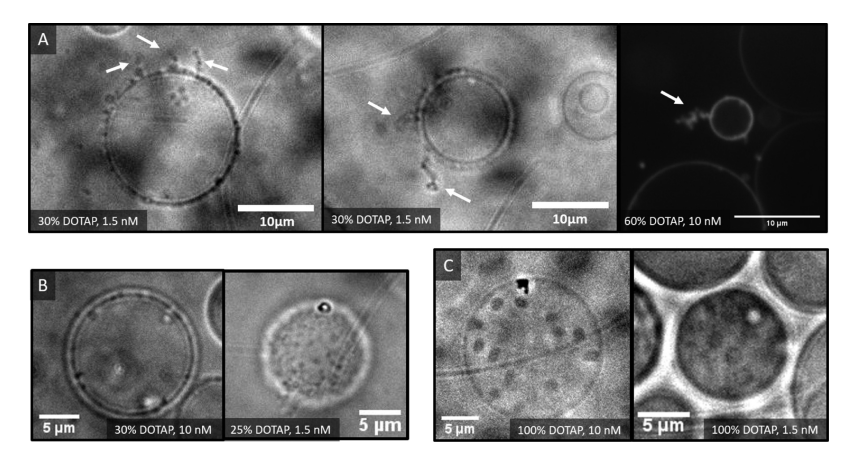


Figure 5. DXR regime: (A) The first two images depict bright-field micrographs of vesicles containing 30 mol % DOTAP. The third image was obtained using a confocal microscope with vesicles containing 60 mol % DOTAP. All three images show examples of external-facing tubules highlighted with arrows and are within the DXR regime. (B) Bright-field micrographs of vesicles containing 25 mol % DOTAP. Particle aggregation is clearly visible as dark mobile spots. These aggregates are typical for vesicles in the strong binding regime. (C) Bright-field micrographs of vesicles containing 100 mol % and 10 mol % DOTAP. Large mobile spots were observed on the surface of the vesicles. This behavior was seen with low $c_{\rm rod}$.

caused by the nanorods accumulating at these junctions due to their ability to bind to both membranes. The adhesive contact area grew over the course of a few minutes until a steady state was reached (Figure 3, yellow region). In samples, where the vesicle concentration was high enough, adhesion led to a solid network of fluid vesicles which we call a "vesicle-gel". The structure of this gel was like that of a dry soap foam with vesicles forming polyhedral configurations when confined by their neighbors. In the case of the vesicle-gel, however, the interior and the continuous phases are both aqueous.

For some trials with 100 mol % DOPC (x = 0), we observed both DAX and DXX behavior at the same rod concentration. No clear boundary between the DXX and DAX was determined for x = 0. We attribute this variation to the fact that different samples may have different rates of mixing in the rods or have different concentrations of vesicles so that the rates of binding and vesicle—vesicle adhesion could vary. By contrast, the other behaviors reported here (DXR, DAR) were highly repeatable and distinct.

DAR Regime: Deformation, Vesicle–Vesicle Adhesion, and Rupture. At intermediate DOTAP content (x = 10-30 mol %), we observed vesicle—vesicle adhesion followed by vesicle rupture (Figure 4). Rupture involved the total collapse of the vesicle's spherical structure, typically in a bursting or shrinking event. In the DAR regime, the rupture process always occurred simultaneously with or after vesicle—vesicle adhesion, resulting in the accumulation of membrane-nanorod aggregates attached to vesicle aggregates.

The progression of events in this regime consisted of first the formation of the vesicle gel within the first few minutes of the experiment. Over time, individual vesicles in the gel cluster burst suddenly. The destruction process was most often very fast (<500 ms; see Figure 4A) but a few events (<1 out of 1000) happened more slowly over a few seconds. The fraction of vesicles destroyed and the rate of vesicle destruction events both varied with $c_{\rm rod}$ and x. Figure S4 shows time sequences of the destruction process for two different samples with x = 10 mol % and $c_{\rm rod} = 1.5$ and 10 nM.

In some vesicles within DAR, we could see dark aggregates that diffused on the surface of the vesicles. These dark mobile aggregates were enriched in rods (as was clear from the scattering) and were too small for us to resolve their size (Figure

S2C). These aggregates were visible in samples with x = 10 mol % and $c_{\rm rod} \le 10$ nM but not when $c_{\rm rod} > 10$ nM.

The DAR regime depended on the membrane excess area as well as $c_{\rm rod}$. The dependence on $c_{\rm rod}$ is evident in vesicles with x=30 mol %: we found a crossover from DXR to DAR by increasing $c_{\rm rod}$ from 1.5 nM to 10 nM. Increasing the vesicle excess area (by making them floppy) drove a reverse crossover, from DAR to DXR, at x=10 mol % and $c_{\rm rod}=1.5$ nM, as well as at x=30 mol % and $c_{\rm rod}=10$ nM. The dependence on $c_{\rm rod}$ and excess membrane area will be addressed in the Discussion section. No other membrane deformation or systematic variation of morphologies were found in samples in the DAR regime.

DXR Regime: Deformation and Rupture. At still higher x, we observed a crossover to a new behavior, consisting of destruction of individual vesicles without vesicle—vesicle adhesion. In this DXR regime, vesicles were destroyed individually in a multistage process (Figure 4B, Supporting Information Video S1, S2, S3). We emphasize that the concentration of vesicles was the same throughout the state diagram and that vesicles had ample opportunity to adhere. We regularly observed vesicles colliding with each other, being pushed into one another via convective flows, or layered on top of one another without any evidence of vesicle adhesion. The absence of vesicle—vesicle adhesion indicated a true lack of adhesive forces.

The process of destruction in the DXR regime was common for hundreds of different vesicles over dozens of different samples varying in x, c_{rod} , and membrane excess area. During the process of destruction, we observed no change in vesicle morphology for a period of time ranging from seconds to tens of minutes depending on c_{rod} (more rods result in a faster response), followed by a sudden drop in size, and then immediately followed by a slow and steady decrease in size until the final rupture (Supporting Information Video S2). Starting radii were typically 5–25 μ m and the magnitude of the sudden drop ranged from $1-10 \mu m$ in roughly 500-1000 ms. In a minority of cases, the vesicle did not survive this sudden drop in radius and instead ruptured at this step. Most vesicles, however, survived the initial drop then showed a steady decrease in the radius over a typical duration of several seconds to minutes. The rate of shrinkage depended on x and c_{rod} ; this dependence will be discussed further below. Within a given fieldof-view, vesicles close to each other tended to shrink at similar rates. As the vesicles shrank, they developed nanorod-rich dark mobile aggregates, which diffused along the surface of the vesicle (Figure 5B). (Some vesicles had a dark mobile aggregate formation before the jump, but the feature was universal after the jump.) In cases of low $c_{\rm rod}$ (<30 nM), roughly one in 100 vesicles developed tubules in addition to the dark mobile aggregates (Figure 5A). Finally, the vesicles underwent complete destruction, wherein at some small radius the vesicles unfurled into a contorted mass of lipid membrane and nanorods, with tubule-like tendrils at its periphery. This process is outlined in Figure 4 and a video is included in the Supporting Information. Examples of the final shape of the lipid-nanorod mass are included in Figure 3 for various combinations of x and $c_{\rm rod}$.

Within the DXR regime, the sequence of steps did not depend on x, vesicle size, or membrane excess area. In rare cases, the vesicle burst immediately after the sudden drop in radius (no discernible shrinkage process). In other rare cases, we observed the slow shrinkage and spots but no sudden drop in radius preceding it; in such cases, the radius drop might have happened out of frame.

The average rate of area contraction (Figure 6) was measured for vesicle populations of x = 30, 60, and 100 mol % DOTAP and

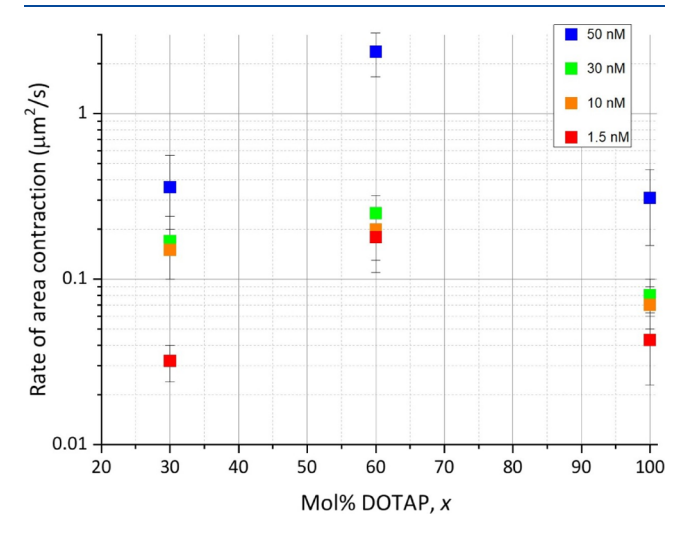


Figure 6. Plot of the average rate of area contraction versus mol % DOTAP in the membrane for vesicles being destroyed via the binding of nanorods. Colors correspond to $c_{\rm rod}$: blue for 50 nM, green for 30 nM, orange for 10 nM, and red for 1.5 nM.

 $c_{\rm rod}=1.5,\,10,\,30,\,$ and 50 nM for both osmotically balanced and floppy vesicles. (Plots of surface area vs. time are in Figure S5.). The average rate of contraction was found by tracking the radius of the vesicle frame-by-frame during the shrinking process after the jump and before final rupture. We observed that the rate of shrinkage depended both on x and $c_{\rm rod}$. For higher $c_{\rm rod}$, the rate of shrinking increased universally for all x. The dependence on x, however, was nonmonotonic with the fastest shrinkage rates found at $x=60\,{\rm mol}\,\%$ across all $c_{\rm rod}$. We are unable to account for this peak in the rate.

We now describe the main structural features in more detail, that is, the dark mobile aggregates, large (\sim 2 μ m) mobile spots, tubules, and the final unfurled rod/membrane structure. The dark mobile aggregates described above were similar in size to the microscope resolution limit and thus, their true size cannot be measured accurately. The dots appeared bright under dark-

field imaging, indicating that they were enriched with nanorods (Figure S2). We never observed particle aggregates in solution and only found these features on vesicles that experienced destruction (DAR and DXR). These observations indicate an attractive interaction between the like-charged nanorods that was mediated by the deformed membrane. (Further evidence for membrane-mediated attraction came from cryo-EM, described below.) Throughout the destruction process, these aggregates remained mobile on the vesicles' surfaces. As the vesicles shrank the concentration of aggregates increased with no observable change in their size. Every vesicle in the DXR regime that underwent destruction during the duration of the experiment had dark mobile aggregates in conjunction with surface shrinking.

Large mobile spots were observed in some DXR vesicles with low to moderate c_{rod} . These spots were approximately 2 μ m in diameter with dark edges. We observed them forming, fading, and diffusing on the surface of some vesicles for several minutes, prior to the drop in radius (Figure 5C, Supporting Information Video S5). They could be seen fading in and out on the surface of the vesicle, but no merging events were observed. They differed from the small dark aggregates in several respects: by their larger size, weaker optical contrast, noncircular shape, their presence prior to the drop in radius, and their disappearance after the radius drop. Their appearance and then disappearance also distinguished them from internalized vesicles, which we sometimes observed and were quite distinct. Large spots occurred on a minority of vesicles at low c_{rod} ; by contrast, the dark aggregates were common among all vesicles in DXR. In our dark-field experiments, we did not observe the large spots, indicating that the density of nanorods in these spots was similar to the average density of rods on the surrounding membrane (and much lower than the rod density in the dark aggregates described previously). These features indicate that some larger scale structures formed due to membrane-mediated interactions of the nanorods, which we will discuss below. These spots were not a universal behavior of vesicles in the DXR regime and seemed to require slower binding of nanorods onto the membrane to form.

Tubules formed in the DXR regime only for $c_{\rm rod}$ < 30 nM. (See Figure S3.). A similar trend was found in the DXX regime: tubules only formed at low $c_{\rm rod}$, suggesting that tubule formation can be frustrated by the presence of too many nanorods. The lack of tubules in the DAR and DAX regimes also suggests that tubule formation was frustrated by the formation of the vesicle gel. In contrast to tubules observed in the DXX regime, tubules formed in DXR were small, $2-10~\mu{\rm m}$ in length and $1-2~\mu{\rm m}$ in diameter, and almost exclusively external.

The final stage of the membrane rupture process was complete vesicle destruction, resulting in a contorted mass of lipid and nanorods with small protrusions on the periphery (e.g., Figure 3). The typical diameter was approximately 2–5 μ m. There was no evidence of correlation between the vesicle size or DOTAP content and the final structure. There was some variation in the structure of the final mass as a function of $c_{\rm rod}$: when $c_{\rm rod}$ = 75 nM, the masses were more compact with smaller external protrusions. Additionally, for low $c_{\rm rod}$, the final mass was less compact and more likely to be slightly elongated (Figure 3).

Cryo-EM at High x and c_{rod} . We used a cryogenic transmission electron microscope to directly image the membrane-rod morphologies with nanoscale precision. Images were taken from 1 to 5 μ m under focus. The cryogenic preparation preserves the arrangement of the rods and

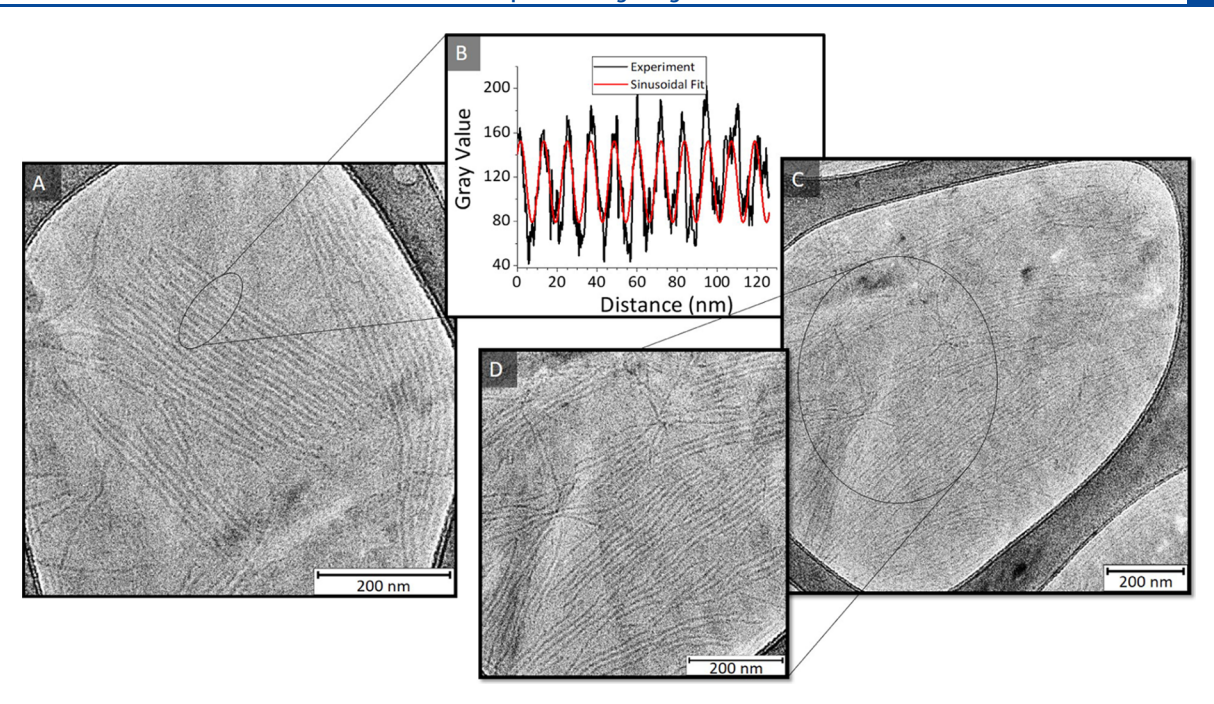


Figure 7. Cryo-TEM images of (A) DNA origami nanorods bound to 100 mol % DOTAP destroyed vesicles incubated for 5 days. When bound to the membrane the nanorods form bundles. (B) Pixel intensity *vs* position perpendicular to the rod axis, showing a periodic spacing of 11.7 nm. (C,D) DNA origami nanorods bound to 100 mol % DOTAP destroyed vesicles incubated for 5 days. Defects in the form of nanorod asters were found among the aligned rods bound to the membrane.

membrane, so that these images give a high-resolution snapshot of the structure. Figure 7 depicts cryo-TEM micrographs of a sample with $x=100 \, \mathrm{mol} \, \%$ DOTAP and $c_{\mathrm{rod}}=75 \, \mathrm{nM}$ and left in suspension for 5 days. (In Figure 2, this sample is represented by the yellow star). We also obtained control images by observing regions of the grid that were devoid of the sample material. These control areas presented only amorphous ice suspended by the lacey carbon grid allowing us to compare the contrast against areas with the sample. This confirmed that the background intensity value behind the rods in our sample images was in fact the lipid membrane and not ice, as they were significantly darker (Figure S6B). It should also be noted that the dark curved edges surrounding the regions with rods are the edge of the lacey carbon that composes the grid. The gaps in the mesh are truly holes with only the supported film of the sample.

The images show nanorods bound to the membrane with high surface coverage and in-plane-ordered patterns of two distinct and common types: parallel rafts and radially oriented asters. We defined parallel rafts as consisting of nanorods where at least half the length lay parallel to another rod that was within 10 nm. Rafts were typically composed of roughly a dozen evenly spaced rods aligned approximately tip-to-tip. By fitting the intensity values along the width of the raft, we found a center-to-center spacing of 11.73 ± 0.02 nm (Figure 7B). In other areas of the sample, we saw a different form of in-plane ordering: aster-like arrays. Nanorods in asters were defined by having one end within a small circular region of the sample (roughly 10 nm across) with the rod extending radially outward from that point. The average length of rods within the asters was observed to be 203 ± 25 nm, half the full length of the rods; we will discuss this point below.

Figure S7 shows a histogram of the population of each type of the rod configuration in the sample, with parallel being the most common and asters the second. To account for all the observed rods, we added two additional categories: overlaid rods were those that lay across parallel-aligned rods. These were readily identified as a single rod lying askew across a bulk of rods. The last case includes all the others, primarily rods that were isolated from other rods.

What is remarkable about all these configurations is that these rods were like-charged and should repel each other. Figure S6A shows a cryo-TEM micrograph of the same nanorods in solution without a membrane. These rods had random orientations with respect to each other. The existence of organized structures and rod packings is strong evidence for membrane-mediated attractive interactions between the rods. We return to this point in the Discussion below.

DISCUSSION

Mechanism of Adhesion and Estimates of Crossovers to Deep and Complete Wrapping. Our results show that nanorod binding induced a variety of membrane morphologies, determined by particle-membrane adhesion strength (DOTAP fraction), particle concentration $c_{\rm rod}$, and membrane excess area (controlled by osmolarity). The primary behaviors observed were membrane deformation (D), vesicle—vesicle adhesion (A), and vesicle rupture (R). We observed well-defined regions in the parameter space with these behaviors and sharp transitions between them. Moreover, we observed deformed membrane morphologies such as tubulation, textured surfaces, small dark aggregates, and large aggregates.

The prominent features of our observations arose from the binding of the rods to the membrane driven by the electrostatic double-layer attraction between them. We tuned the adhesion energy per area, ω , between particles and the membrane by means of DOTAP fraction, x. Direct evidence of particle adhesion is provided by the dark-field experiment (Figure S2), which show increased brightness on the surface of vesicles after the introduction of rods. We note that rods are also bound to 100% DOPC vesicles (x = 0) and caused deformation.

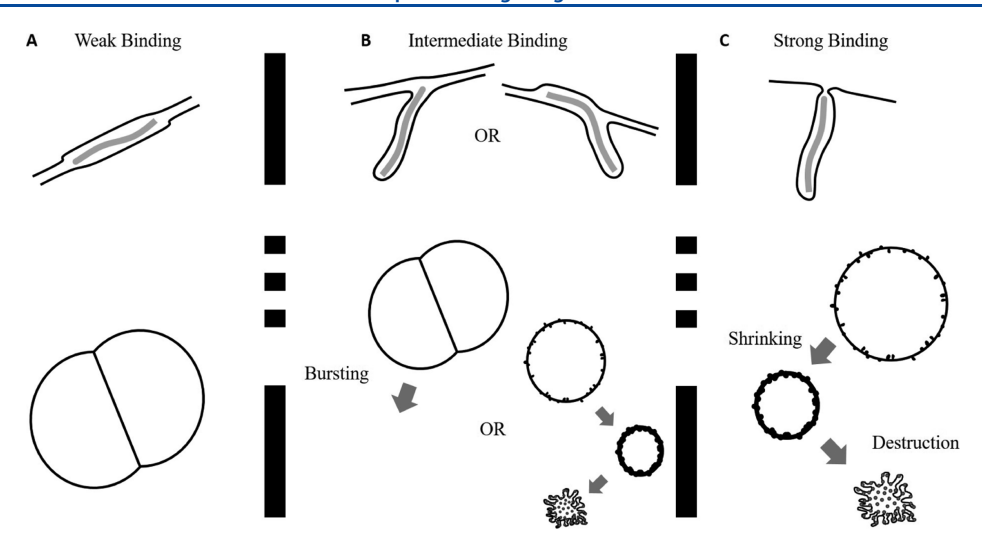


Figure 8. Illustration of the wrapping configurations of rods by the membrane and their association with collective phenomena. (A) At low ω, weak binding was observed leading to adhesion and sometimes deformation (DXX and DAX). (B) With the increase of ω, a crossover to deep wrapping was observed (B). The membrane area taken up led to rupture (DAR). (C) At still higher ω, a second crossover to complete wrapping was found, which still led to rupture. Here, the rod had no exposed part, so adhesion was absent (DXR).

This seems surprising in view of the findings that DOPC vesicles have a slightly negative electrostatic (zeta) potential of -9 mV (electrophoretic mobility with 0.1 mM NaCl)^{41,42} and might therefore be expected to repel the negatively charged nanorods. We attribute the binding in this case to the static dipole of the zwitterionic PC headgroup, which can reorient to attract the charged objects of either sign. 43,44 Previously, we found that anionic silica particles were also able to bind to DOPC vesicles. 26,45,46 With increasing x, we anticipate that ω will increase monotonically but not necessarily linearly because the cationic lipids might preferentially accumulate near the rods. Prior theory showed that this accumulation substantially increases the binding free energy of DNA molecules on cationic membranes when x is in the range of 0.2-0.4 and that the binding energy is approximately constant when x > 0.6. The rods described here have a higher effective charge density and binding energy but may have a qualitatively similar trend of ω with x.

When a rod binds, the membrane bends around it in order to increase the adhesion area. This deformation leads to the observed interactions among the rods (Figure 6) and leads to further deformations as reported in Figure 2. The membrane deformation can be explained from a continuum approach, in which the energy of rod-membrane adhesion competes with the energy cost of bending and stretching the membrane and the loss of entropy when a free rod binds to a membrane. The bending energy predominates over stretching when $a^2\tau/\kappa \ll 1$, where τ is the tension. For our system, this is valid in the initial case when the vesicles are floppy ($\tau \ll 1 \text{ mN/m}$), but this dimensionless ratio is approximately 1 when the tension approaches the lysis point ($\sim 10 \text{ mN/m}$). From here on, we assume that the vesicle is not near lysis and the energy of bending predominates. The energy of bending the membrane can be determined via the Helfrich model⁴⁷ and depends on the size and shape of the particle. 15,48 In the case of the perfectly rigid rod-shaped nanoparticles, simulations predicted three wrapping configurations: shallowly wrapped, deeply wrapped, and completely wrapped, for rods with rounded ends and small aspect ratios (length over width ranging from 1 to 3). 25,34 The existence of three wrapping configurations was ascribed to the

inhomogeneous curvature on the nanoparticle surface. Initial binding occurs even with vanishingly small adhesion strength. 25,49 With increasing ω , the first bound state found in simulations was shallow wrapping, in which the rod lies parallel and the membrane slightly deforms around it. The transition from shallow wrapped to deep wrapping requires the rod to tilt normal to the membrane so that one end of the rod is wrapped. This transition is tension-dependent; it shifts to higher ω with increased τ , as it does for spheres. At higher ω , there is a second transition to complete wrapping, in which no surface of the rod is exposed. The neck where the membrane closes around the rod is a minimal surface (catenoid) and does not contribute to the membrane bending energy. Transitions between these configurations are predicted to be discontinuous in the binding energy.

We can estimate where these transitions occur using continuum theory, which can apply at scales as small as a few nm. ⁵⁰ We assume perfectly rigid, cylindrical rods with hemispherical ends. The dimensions of the rod are characterized by its radius, *a*, and the length, *l*, of the cylindrical part. As often done, we treat the adhesion as arising from attractive forces with a range much smaller than *a*. We summarize the results here and refer the reader to the supplementary section (Figure S8) for

details. When $\frac{a^2\omega}{\kappa} < \frac{2 + \frac{1}{2}\frac{1}{a}}{1 + \frac{1}{a}}$, we expect the rod to lie flat on the

membrane with weak deformation (Figure 8a), as the energy to wrap one hemispherical end is too high. This regime should correspond to adhesion and deformation but not rupture (DXX

or DAX). When
$$\frac{2+\frac{1}{2a}}{1+\frac{1}{a}} \le \frac{a^2\omega}{\kappa} < 2$$
, the energy to wrap the

cylindrical body is sufficient to compensate the cost of wrapping one hemispherical end. Therefore, the minimum energy state has the entire rod wrapped except one end (called "deep wrapping", Figure 8b). This configuration should lead to adhesion between vesicles because of the exposed rod end and also vesicle rupture because of the large area taken up by each rod. This behavior corresponds to the DAR regime in experiments. Finally, when $\frac{a^2\omega}{\kappa} \geq 2$, adhesion overcomes the energy cost of wrapping the ends and the rod is completely

wrapped (Figure 8c). There should be no exposed rod and hence no vesicle—vesicle adhesion: this behavior corresponds to DXR.

The sequence of partially and fully wrapped configurations from this simple, single-particle model nicely captures the experimentally discovered sequence of DXX or DAX to DAR and DXR with increasing ω . Quantitatively, however, the model predicts a very narrow range of DAR because the rod aspect ratio

l/a is of the order of 100, so that $\frac{2 + \frac{1}{2a}}{1 + \frac{1}{a}} \approx 2$. This discrepancy

may come from having many rods present (which shifts the wrapping transition for the case of spheres²⁶ and may do the same for rods). It might also be that the ability of the rods to bend is important and may widen the regime of deep wrapping. In our model and previous reports,^{25,34} the rods were taken to be perfectly rigid. We return to this point below in the context of aster-like formations seen in cryo-TEM images.

We organize our remaining discussion into weak, intermediate, and strong binding before turning to membrane-mediated forces between rods and then to the dynamics of the rupture process.

Discussion of Weak, Intermediate, and Strong Binding **Regimes.** First, we consider the case of weak binding at low x(Figure 8a). Because the rods are hydrophilic and highly charged, they remain at the surface of the membrane rather than in the hydrophobic core: that is., they bind to the surface. When the adhesion of the particles to the membrane is too weak to wrap the high curvature ends of the rod, the theory predicts rods to be shallowly wrapped in equilibrium.²⁵ The two states associated with the lowest binding energy are DXX and DAX, which are present for membranes with x < 10 mol % DOTAP. In the regime of DXX, shallow wrapping deforms the membrane and caused tubules, elongated structures, and textured surfaces. Tubules and elongated shapes are plausibly due to cylindrical curvature induced on the membranes surface by the nanorods. The onset of adhesion in DAX is readily explained by a rod binding to one membrane, leaving one side exposed and able to bind to a second membrane, thus forming an adhesive bridge and leading to a macroscopic gel. A similar result was found using spherical particles with weak binding.²⁶ DAX tends to be found with higher c_{rod} , suggesting that the vesicle-vesicle adhesion energy depends on c_{rod} , which agrees with a published statistical mechanical model of particle-based adhesion between surfaces.⁵¹ We see indistinguishable behavior for the equiosmolar and floppy (excess-area) vesicles in this regime. Tubules existed also in the DXR regime but only for small rod concentrations. The dependence on low particle concentration suggests that tubule formation can be interrupted or frustrated by the jamming of particles or by increased membrane tension due to particle binding and area consumption or due to vesicle vesicle adhesion. Further discussion on the formation of tubules is continued below when compared to tubules formed in the DXR regime.

At intermediate adhesion energy ω , our observed transition to DAR (the onset of destruction) is attributed to the transition from shallow to deep wrapping at the individual particle scale (Figure 8b). This configuration leaves a portion of the rod exposed, thus allowing it to form an adhesive bridge between vesicles resulting in a bulk vesicle gel. Unlike the shallow wrapping, however, deeply wrapped rods drastically deform the membrane and consume a substantial amount of the projected surface area. This area consumption increases membrane

tension, resulting in the runaway destruction of vesicles. Our key experimental observation that supports the deep-wrapping hypothesis is the sharp transition in the parameter space between samples with no rupture and samples with rupture, which is consistent with the predicted sharp transition from loose to deep wrap. ^{15,25}

Lastly, we consider the transition to rupturing without adhesion (DXR) at highest adhesion energy ω . We hypothesize that this regime corresponds to the complete wrapping of the rods (Figure 8c). When a rod is completely enveloped by the membrane there is no exposed rod available to form an adhesive bridge, thus turning off vesicle-vesicle adhesion. The hypothesis of complete wrapping is further supported by several experimental observations. First, the transition from DAR to DXR is sharp, as is predicted for the single rod deep-to-complete wrap transition. 25 Second, DXR occurred at the maximum x for each c_{rod} , corresponding to the limit of the strongest ω . Third, adding excess area to the vesicles (by exposing them to hyperosmotic conditions) favored DXR over DAR (at x = 10%, $c_{\rm rod} = 1.5$ nM and at 30%, 10 nM). We hypothesize that adding excess areas made it easier for the membrane to completely wrap the rods that were bound. Finally, a higher c_{rod} suppressed DXR and favored DAR, which indicates that a high concentration of bound rods suppressed complete wrapping, either because the rods take up a large amount of the membrane and significantly raise the membrane tension or because steric hindrance among the bound rods prevents their being fully wrapped.

Tubules formed at low $c_{\rm rod}$ but did not form at high $c_{\rm rod}$ (which was the case in DXX). Tubules in the DXR regime were typically directed outward, $1-2~\mu{\rm m}$ in diameter and $2-10~\mu{\rm m}$ long. They may form due to the cylindrical curvature induced on the membrane by the binding of the rods. The tubules formed in the DXR regime were typically smaller than those seen in DXX, and the DXX regime had both inward- and outward-pointing tubules. Previous studies showed that particles or proteins that bind on the exterior leaflet without wrapping can drive tubules to extend outward, driven by a lateral pressure arising from steric interactions among the particles or proteins. S2-54 We find the presence of both inward and outward tubules in the DXX regime to be surprising.

Discussion of Membrane-Mediated Interactions among Rods. The dark mobile aggregates observed in the DAR and DXR regimes can also be explained by the deep-to-complete wrapping transition. The dark mobile aggregates are nanorod-enriched spots (Figure S2). Because the nanorods repel one another in the suspension (due to the electrostatic double-layer interaction), the aggregation must be induced by membrane deformation. Previous theory shows that the membrane induces lateral attraction between nanorods strongly bound to the membrane and repulsion between weakly bound ones; ⁵⁵ these predictions are consistent with indirect evidence from the condensation of flexible DNA. ^{29,56} In more rigid fd viruses, experiments found linear tip-to-tip aggregates, ²⁸ though these might not have been strongly bound and wrapped.

The cryo-TEM images (Figure 7) show a striking organization of the bound nanorods in the case of strong ω and high $c_{\rm rod}$ (x=100 mol % and $c_{\rm rod}=75$ nM). We found clear in-plane parallel ordering of the nanorods as well as aster-like configurations. We found a comparable number of rods in each of those two configurations. The parallel rods had a center-to-center spacing of 11.73 ± 0.02 nm.

While the evidence for rod-rod attraction is very striking, we note that this result may also resolve a conflict in prior

theoretical work. For the case of infinitely long and rigid rods on the same side of the membrane, there are predictions of pairwise repulsion between the rods for weak deformation and either repulsion^{57,58} or attraction⁵⁵ with strong deformation. (Our results agree with the latter.) For finite-length rods, simulations demonstrated both repulsive and attractive interactions between rods depending on the orientation of the rods with respect to one another. 59 Muller, et al. predicted that the interaction between rods bound to the membrane to be repulsive for rods on the same side and attractive for rods on opposite leaflets. ⁶⁰ The earlier work, however, treated the rods as infinitely long, so they did not consider the membrane deformation at the rod ends, which may be particularly relevant for monodisperse rods where the tips can align, as our origami rods do to some extent. The earlier theory also considered only the case of two rods, whereas it is known that membrane-mediated interactions can be nonpairwise-additive, so that two might repel while several attract.61 Membrane-mediated interactions among rigid or flexible rods remain a topic for continued investigation.

The aster-like regions seen in the cryo-TEM images were composed of rods that were shorter than the full length. From cryo-TEM images, the average measured rod length in the bulk phase was found to be around 341 ± 50 nm, which roughly matches the designed length of the rods (i.e., 420 nm). Similarly, the mean length in the parallel arrays was 391 ± 25 nm. However, rods in the asters were about half that length, averaging 203 ± 25 nm (Figure S7). Knowing the nature and structure of DNA origami nanorods, it is highly improbable that short rods would form originally (and they were not found in the cryo-TEM images without membranes) or that long rods would be able to break cleanly. Therefore, we suspect that the rest of the rods in these aster-like formations are deflected out of plane, as illustrated in Figure S9. In the lower resolution optical images, we noted short (<1 μ m), outward-forming objects during the destruction process and in the final aggregate structures (Figure 3); we attribute these to the aster-like protrusions seen in cryo-TEM images. Furthermore, these out-of-plane deformations could make ideal nucleation sites for the larger tubules seen on some of the membranes.

Why would rods form aster-like bundles that protrude from the membrane? Perfectly rigid rods that are wrapped at one end but not at both ends (*i.e.*, "deep wrapped") require a large membrane mean curvature. For flexible rods, bending the rod allows the membrane curvature to be spread out over a larger area, which may reduce the energy cost of deformation while still providing substantial adhesion area. Accounting for finite rod flexibility in future simulation studies would be a very informative direction for future works. If our proposed aster structure is borne out, then this mode of deformation may be very important in the nucleation of filopodia (and especially the smaller microspikes) in cells.⁴

Dynamics of the Destruction Process. Single vesicle destruction events were observed for vesicles in the DAR and DXR regimes. During this process, vesicles experienced a sudden drop in the radius, followed by the steady shrinking of the vesicle until its final rupture. The time before the drop was dependent on $c_{\rm rod}$, with higher concentrations resulting in a faster onset of the destruction process. The dependence on $c_{\rm rod}$ implies that the trigger for the drop is a many-particle behavior, requiring some minimum surface coverage. Vesicles within a single field-of-view did not all jump down in radius simultaneously upon the introduction of the nanorods. The sudden drop in the size of individual vesicles happened

stochastically, indicative of a particle nucleation process occurring on the membrane.

The rate of area contraction was found to depend on x and $c_{\rm rod}$. The rate of shrinking increased universally with $c_{\rm rod}$ for all DOTAP fractions measured. This dependence on $c_{\rm rod}$ makes sense if the projected area contraction is driven by the consumption of area by the binding of rods. The flux of rods on the membrane is proportional to $c_{\rm rod}$; as rods bind to and are enveloped by the membrane, the excess area should contract until the membrane can no longer support more rods, causing its final rupture. The measured rate was, however, nonmonotonic with x; the fastest shrinkage rates were found at x = 60 mol % DOTAP across all $c_{\rm rod}$. This is quite surprising as it implies that the shrinkage rate is influenced by some additional mechanism beyond particle flux and envelopment.

Solute exchange across the membrane must occur rapidly to accommodate the projected area contraction. This is particularly striking during the sudden drop in radius where as much as 10% of the vesicle volume is exchanged in less than 500 ms (a mean surface-area reduction rate of approx. 50 μ m²/s). The solution contains sugar that in ordinary unstressed conditions requires hours to permeate 62 and that should require tensions well above the lysis tension to accommodate shrinkage rates above roughly $0.1 \ \mu \text{m}^2/\text{s}$ (as discussed previously). The observation that vesicles can shrink so fast implies water permeation and also rapid sugar permeation, otherwise there would be an osmotic stress. The nucleation and then subsequent closing of nanoscopic pores in the membrane could explain the sudden exchange of the solute required to reduce the volume. The continued binding of rods to the membrane may also enhance solute exchange rates, as reported earlier with nanospheres⁵³ and polymers.⁶³

CONCLUSIONS

In our experiments, we carefully tuned the interactions between lipid bilayer membranes and DNA origami nanorods to understand how nanoparticle adhesion can be used to remodel membranes. Controlling particle shape, membrane tension, particle concentration, and binding strength allowed us to deform the membrane in a variety of unique, repeatable, and definable ways. The ability to control membrane remodeling in this way may lead to the design of novel membrane-based materials.

These results span a large parameter space and show a consistent picture of particle-membrane interactions. We found four distinct membrane morphological behaviors with different combinations of deformation (D), adhesion (A), and rupture (R), or their absence (X). We observed four well-defined primary regimes in the state space (DXX, DAX, DAR, and DXR). Each regime has unique features which distinguish it from the others and have the distinct potential for application. The DAX regime results in a long-lived stable vesicle gel that has a high surface area, a large volume of more than 99% water and an intact closed-cell structure separated by the membrane that is impermeable to solutes. The large surface area can be easily functionalized, and the closed-cell structure should allow for the encapsulation of multiple reagents, which would only react upon the rupture of the gel structure. The DAR regime exhibits gel formation as well as vesicle rupture, which could be utilized to create, hold, and then release cargo at a rate determined by the particle concentration. The DXR regime also exhibits vesicle rupture without the gel formation. Such a mechanism could be used for a triggerable release of cargo from within the vesicle. The crossover between these various responses is controlled by adhesion strength, particle concentration, and membrane tension. This system has the potential for application in a myriad of contexts such as in encapsulation, delivery, and triggered release of cargo on the micron scale. The results might also explain the mechanisms of protein rodlet arrangement in immunosilencing fungal spores, ⁶⁴ binding of filamentous viruses such as Ebola on cells, ¹² as well as formation of filopodia with actin bundles.⁴

The charged lipid composition, x, was the most important parameter in determining the response through its control of the adhesion energy per area, ω . Increasing rod concentration, $c_{\rm rod}$ increased overall response rates and also favored DAR over DXR. The mechanism may have been steric hindrance among bound rods preventing complete wrapping or rapid consumption of excess area leading to tension and suppressing complete wrapping. The excess membrane area was the third control parameter; it caused a more subtle shift in the response by favoring complete wrapping or, on the contrary, suppressing wrapping if the excess area was small.

In earlier works with rod-shaped flexible virus particles (fd virus), Petrova et al. identified three different configurations. As in our work, they varied the membrane charge by mixing DOPC and DOTAP lipids. For the lowest membrane charge (x= 0.01), they observed bound virus particles moving freely on the membrane. With a higher charge and added salt, they found tip-to-tip aggregation. With a higher charge (x > 0.02) and no added salt, they found collapsed virus particles due to either inplane self-interactions (coiling as in the "snail" model) or disassembled viruses. They did not report vesicle destruction at their relatively low DOTAP fractions, which is consistent with our results. Experiments with DNA molecules (as opposed to bundles) also showed snail-like coiling, attributed to membrane wrapping.^{29,56} The fd virus and especially the DNA molecules are quite flexible (the virus has a persistence length of 2.5 ± 0.2 μ m), which might facilitate snail collapse. In our experiments, we found no evidence of snail formation, though it would be difficult to see optically. We did, however, find an aster-like morphology that we attributed to the deep wrapping of the rod ends and a membrane protrusion akin to microspikes in filopodia (Figure S6). Possibly, this morphology also explains the collapsed structure seen with the flexible fd virus. 28 Taken together, these results suggest that the flexibility of the rods is an important parameter in determining the membrane response.

Recent experiments with DNA origami particles, like the ones used here, investigated curved as well as straight rods. 18,30,31 The binding strength was tuned by incorporating a defined number of membrane-anchoring groups on the particles. Curved rods (resembling the banana-shaped BAR protein domain) led to significant vesicle deformation, while straight rods did not. 18 This latter observation differs strikingly from our work, and we attribute the difference to a stronger binding affinity in our system, leading to a crossover from weak binding and deformation to wrapping. The role of the particle shape depends on binding strength, so that a sampling of the $\omega a^2/\kappa$ axis is needed for a complete understanding.

We end with a comparison of the present results to prior studies of spherical nanoparticles. With spherical nanoparticles, a recent report by some of us showed a sharp crossover from adhesion to destruction with increasing electrostatic adhesion strength ω . Weakly bound nanospheres caused the formation of a vesicle gel, while strongly bound nanospheres resulted in the destruction of the vesicles in a process that included the

shrinking of the vesicle size, the formation of dark mobile aggregates, tubules, and pores, and lastly vesicle rupture. In the terms of this paper, the spheres showed a transition from DAX to DXR (rupture without adhesion). Similar to the rod case, this transition corresponded to a transition from weak deformation to complete wrapping at the scale of individual particles when $\omega a^2/\kappa$ was of order 1,²⁶ consistent with a prior theoretical and simulation work with one or a few nanoparticles. 15,17,25,26,46,65 Differences in surface chemistry (especially charge) make it difficult to compare the numerical values for the threshold xvalues for the spheres²⁶ and rods. However, given that the radius of our DNA origami nanorods is quite similar to the radius of the Au-TTMA nanoparticles used previously,²⁶ we anticipate a similar threshold membrane charge density for DXR, which is indeed the case (4 mol % DOPS for the Au-TTMA spheres, < 20 mol % for DNA rods). The presence of tubules is shared with the experimental findings in membranes with a diversity of spherical particles^{26,66-68} or proteins, ^{52,69} virus or DNA origami rods, ^{18,28,70} and other shapes. ^{30,31} It is worth noting that rods give rise to inward- and outward-pointing tubules, with the outward ones being the most prevalent (in contrast to spheres). At the vesicle scale, the greatest difference between rods and spheres appears to be the additional crossover in the latter system to adhesion and rupture, owing to the partial wrapping. The ability to control the interactions between membranes and particles allows us to isolate which effects are governed by particle shape, membrane tension, adhesion strength, and particle concentration.

ASSOCIATED CONTENT

Supporting Information

The Supporting Information is available free of charge at https://pubs.acs.org/doi/10.1021/acs.langmuir.1c00416.

Optical images of specific morphologies and time sequences; a more detailed state diagram; analysis of rod configurations seen in cryo-TEM images; illustration of the proposed aster structure; schematic of the sample cells used; and details of our continuum model for wrapping rods (PDF)

Confocal micrographs of three vesicles in the DXR regime shrinking down and being destroyed; x = 60%, $c_{\text{rod}} = 10$ nM (AVI)

Confocal images of two vesicles in the DXR regime that experience a sudden drop in their size before beginning to shrink and finally being destroyed; x = 60%, $c_{\text{rod}} = 10 \text{ nM}$ (AVI)

Bright-field time lapse of a single vesicle in the DXR regime as it shrinks and is destroyed; x = 30%, $c_{\text{rod}} = 1.5$ nM (AVI)

Bright-field time lapse video of a vesicle in the DXX regime with textured surface; x=0, $c_{\rm rod}=1.5$ nM (AVI) Vesicle in the DXR regime with x=10 mol % DOTAP combined with nanorods with $c_{\rm rod}=10$ nM concentration, showing large mobile spots (AVI)

AUTHOR INFORMATION

Corresponding Author

Anthony D. Dinsmore — Department of Physics, University of Massachusetts Amherst, Amherst, Massachusetts 01002, United States; ⊚ orcid.org/0000-0002-0677-765X; Email: dinsmore@umass.edu

Authors

Sarah E. Zuraw-Weston — Department of Physics, University of Massachusetts Amherst, Amherst, Massachusetts 01002, United States

Mahsa Siavashpouri – Department of Physics, Brandeis University, Waltham, Massachusetts 02454, United States

Maria E. Moustaka — Department of Physics, Brandeis University, Waltham, Massachusetts 02454, United States; orcid.org/0000-0003-4479-1775

Thomas Gerling – Department of Physics, Technical University of Munich, Garching D-85748, Germany

Hendrik Dietz – Department of Physics, Technical University of Munich, Garching D-85748, Germany

Seth Fraden – Department of Physics, Brandeis University, Waltham, Massachusetts 02454, United States

Alexander E. Ribbe — Department of Polymer Science and Engineering, Silvio O. Conte National Center for Polymer Research, University of Massachusetts Amherst, Amherst, Massachusetts 01003, United States; orcid.org/0000-0002-9924-3429

Complete contact information is available at: https://pubs.acs.org/10.1021/acs.langmuir.1c00416

Author Contributions

The manuscript was written through contributions of all the authors. All the authors have given approval to the final version of the manuscript.

Notes

The authors declare no competing financial interest.

■ ACKNOWLEDGMENTS

We thank Arash Manafirad and Rui Cao for helpful discussions and their technical assistance. We acknowledge the National Science Foundation (NSF)-funded Materials Research Science and Engineering Center (MRSEC) on Bioinspired Soft Materials for awarding the grant (DMR-2011486). We also acknowledge partial funding through the NSF grant CBET-1803797 from the NSF Division of Chemical, Biological, Environmental and Transport Systems. SZW acknowledges partial support through the Spaulding-Smith Fellowship program on site at the University of Massachusetts, United States.

ABBREVIATION

GUVs, giant unilamellar vesicles; TEM, transmission electron microscopy; XXX, no deformation—no adhesion—no rupture; DXX, deformation—no adhesion—no rupture; DAX, deformation—adhesion—rupture; DXR, deformation—no adhesion—rupture

REFERENCES

- (1) van Meer, G.; Voelker, D. R.; Feigenson, G. W. Membrane lipids: where they are and how they behave. *Nat. Rev. Mol. Cell Biol.* **2008**, *9*, 112.
- (2) Zimmerberg, J. Membrane Biophysics. Curr. Biol. 2006, 16, R272.
- (3) Shibata, Y.; Voeltz, G. K.; Rapoport, T. A. Rough sheets and smooth tubules. *Cell* **2006**, *126*, 435–439.
- (4) Mellor, H. The role of formins in filopodia formation. *Biochim. Biophys. Acta Mol. Cell Res.* **2010**, *1803*, 191–200.
- (5) Keren, K. Cell motility: the integrating role of the plasma membrane. Eur. Biophys. J. Biophys. Lett. 2011, 40, 1013-1027.

- (6) Kay, R. R.; Langridge, P.; Traynor, D.; Hoeller, O. Changing directions in the study of chemotaxis. *Nat. Rev. Mol. Cell Biol.* **2008**, *9*, 455–463.
- (7) Svitkina, T. The Actin Cytoskeleton and Actin-Based Motility. Cold Spring Harbor Perspect. Biol. 2018, 10, a018267.
- (8) Richards, D. M.; Endres, R. G. How cells engulf: a review of theoretical approaches to phagocytosis. *Rep. Prog. Phys.* **2017**, *80*, 126601.
- (9) Johannes, L.; Parton, R. G.; Bassereau, P.; Mayor, S. Building endocytic pits without clathrin. *Nat. Rev. Mol. Cell Biol.* **2015**, *16*, 311–321
- (10) McMahon, H. T.; Gallop, J. L. Membrane curvature and mechanisms of dynamic cell membrane remodelling. *Nature* **2005**, *438*, 590–596.
- (11) Chithrani, B. D.; Chan, W. C. W. Elucidating the mechanism of cellular uptake and removal of protein-coated gold nanoparticles of different sizes and shapes. *Nano Lett.* **2007**, *7*, 1542.
- (12) Zhang, Q.; Tian, F.; Wang, F.; Guo, Z.; Cai, M.; Xu, H.; Wang, H.; Yang, G.; Shi, X.; Shan, Y.; Cui, Z. Entry Dynamics of Single Ebola Virus Revealed by Force Tracing. ACS Nano 2020, 14, 7046—7054.
- (13) Alipour, E.; Halverson, D.; McWhirter, S.; Walker, G. C. Phospholipid Bilayers: Stability and Encapsulation of Nanoparticles. *Annu. Rev. Phys. Chem.* **2017**, *68*, 261–283.
- (14) Nikoleli, G.-P.; Nikolelis, D.; Siontorou, C.; Nikolelis, M.-T.; Karapetis, S. The Application of Lipid Membranes in Biosensing. *Membranes* **2018**, *8*, 108.
- (15) Deserno, M. Elastic deformation of a fluid membrane upon colloid binding. *Phys. Rev. E* **2004**, *69*, 031903.
- (16) Le Bihan, O.; Bonnafous, P.; Marak, L.; Bickel, T.; Trépout, S.; Mornet, S.; De Haas, F.; Talbot, H.; Taveau, J.-C.; Lambert, O. Cryoelectron tomography of nanoparticle transmigration into liposome. *J. Struct. Biol.* **2009**, *168*, 419.
- (17) Bahrami, A. H.; Raatz, M.; Agudo-Canalejo, J.; Michel, R.; Curtis, E. M.; Hall, C. K.; Gradzielski, M.; Lipowsky, R.; Weikl, T. R. Wrapping of nanoparticles by membranes. *Adv. Colloid Interface Sci.* **2014**, 208, 214–224.
- (18) Franquelim, H. G.; Khmelinskaia, A.; Sobczak, J. P.; Dietz, H.; Schwille, P. Membrane sculpting by curved DNA origami scaffolds. *Nat. Commun.* **2018**, *9*, 811.
- (19) Reynwar, B. J.; Illya, G.; Harmandaris, V. A.; Müller, M. M.; Kremer, K.; Deserno, M. Aggregation and vesiculation of membrane proteins by curvature-mediated interactions. *Nature* **2007**, *447*, 461.
- (20) Adriani, G.; de Tullio, M. D.; Ferrari, M.; Hussain, F.; Pascazio, G.; Liu, X.; Decuzzi, P. The preferential targeting of the diseased microvasculature by disk-like particles. *Biomaterials* **2012**, *33*, 5504–5513.
- (21) Yu, Q.; Dasgupta, S.; Auth, T.; Gompper, G. Osmotic Concentration-Controlled Particle Uptake and Wrapping-Induced Lysis of Cells and Vesicles. *Nano Lett.* **2020**, *20*, 1662–1668.
- (22) Reynwar, B. J.; Deserno, M. Membrane-mediated interactions between circular particles in the strongly curved regime. *Soft Matter* **2011**, *7*, 8567.
- (23) Qualmann, B.; Koch, D.; Kessels, M. M. Let's go bananas: revisiting the endocytic BAR code. *EMBO J.* **2011**, *30*, 3501–3515.
- (24) Linklater, D. P.; Baulin, V. A.; Le Guével, X.; Fleury, J. B.; Hanssen, E.; Nguyen, T. H. P.; Juodkazis, S.; Bryant, G.; Crawford, R. J.; Stoodley, P.; Ivanova, E. P. Antibacterial Action of Nanoparticles by Lethal Stretching of Bacterial Cell Membranes. *Adv. Mater.* **2020**, 32, 2005679.
- (25) Dasgupta, S.; Auth, T.; Gompper, G. Shape and Orientation Matter for the Cellular Uptake of Nonspherical Particles. *Nano Lett.* **2014**, *14*, 687–693.
- (26) Zuraw-Weston, S.; Wood, D. A.; Torres, I. K.; Lee, Y.; Wang, L.-S.; Jiang, Z.; Lázaro, G. R.; Wang, S.; Rodal, A. A.; Hagan, M. F.; Rotello, V. M.; Dinsmore, A. D. Nanoparticles binding to lipid membranes: from vesicle-based gels to vesicle tubulation and destruction. *Nanoscale* **2019**, *11*, 18464–18474.

- (27) Spangler, E. J.; Laradji, M. Discontinuous wrapping transition of spherical nanoparticles by tensionless lipid membranes. *J. Chem. Phys.* **2020**, *152*, 104902.
- (28) Petrova, A. B.; Herold, C.; Petrov, E. P. Conformations and membrane-driven self-organization of rodlike fd virus particles on freestanding lipid membranes. *Soft Matter* **2017**, *13*, 7172–7187.
- (29) Herold, C.; Schwille, P.; Petrov, E. P. DNA Condensation at Freestanding Cationic Lipid Bilayers. *Phys. Rev. Lett.* **2010**, *104*, 148102.
- (30) Czogalla, A.; Kauert, D. J.; Franquelim, H. G.; Uzunova, V.; Zhang, Y.; Seidel, R.; Schwille, P. Amphipathic DNA Origami Nanoparticles to Scaffold and Deform Lipid Membrane Vesicles. *Angew. Chem., Int. Ed.* **2015**, *54*, 6501–6505.
- (31) Czogalla, A.; Franquelim, H. G.; Schwille, P. DNA Nanostructures on Membranes as Tools for Synthetic Biology. *Biophys. J.* **2016**, *110*, 1698–1707.
- (32) Gratton, S. E. A.; Ropp, P. A.; Pohlhaus, P. D.; Luft, J. C.; Madden, V. J.; Napier, M. E.; DeSimone, J. M. The effect of particle design on cellular internalization pathways. *Proc. Natl. Acad. Sci. U.S.A.* **2008**, *105*, 11613–11618.
- (33) Champion, J. A.; Mitragotri, S. Role of target geometry in phagocytosis. *Proc. Natl. Acad. Sci. U.S.A.* **2006**, *103*, 4930.
- (34) Bahrami, A. H. Orientational changes and impaired internalization of ellipsoidal nanoparticles by vesicle membranes. *Soft Matter* **2013**, *9*, 8642–8646.
- (35) Paasonen, L.; Laaksonen, T.; Johans, C.; Yliperttula, M.; Kontturi, K.; Urtti, A. Gold nanoparticles enable selective light-induced contents release from liposomes. *J. Controlled Release* **2007**, *122*, 86–93
- (36) Herold, C.; Chwastek, G.; Schwille, P.; Petrov, E. P. Efficient Electroformation of Supergiant Unilamellar Vesicles Containing Cationic Lipids on ITO-Coated Electrodes. *Langmuir* **2012**, *28*, 5518–5521.
- (37) Siavashpouri, M.; Wachauf, C. H.; Zakhary, M. J.; Praetorius, F.; Dietz, H.; Dogic, Z. Molecular engineering of chiral colloidal liquid crystals using DNA origami. *Nat. Mater.* **2017**, *16*, 849.
- (38) Gerling, T.; Kube, M.; Kick, B.; Dietz, H. Sequence-programmable covalent bonding of designed DNA assemblies. *Sci. Adv.* **2018**, *4*, No. eaau1157.
- (39) Andelman, D. Electrostatic Properties of Membranes: The Poisson-Boltzmann Theory. In *Handbook of Biological Physics*; Lipowsky, R., Sackmann, E., Eds.; Elsevier Science B.V, 1995; Vol. 1, pp 603–642.
- (40) McLaughlin, S. The Electrostatic Properties of Membranes. *Annu. Rev. Biophys. Biophys. Chem.* **1989**, *18*, 113–136.
- (41) Needham, D.; Zhelev, D. Use of Micropipet Manipulation Techniques to Measure the Properties of Giant Lipid Vesicles. In *Perspectives in Supramolecular Chemistry: Giant Vesicles*; Luisi, P. L., Walde, P., Eds.; John Wiley & Sons: Hoboken, NJ, 2007.
- (42) Maity, P.; Saha, B.; Kumar, G. S.; Karmakar, S. Binding of monovalent alkali metal ions with negatively charged phospholipid membranes. *Biochim. Biophys. Acta, Biomembr.* **2016**, *1858*, 706–714.
- (43) Wang, B.; Zhang, L.; Bae, S. C.; Granick, S. Nanoparticle-induced surface reconstruction of phospholipid membranes. *Proc. Natl. Acad. Sci. U.S.A.* **2008**, *105*, 18171–18175.
- (44) Haugen, A.; May, S. The influence of zwitterionic lipids on the electrostatic adsorption of macroions onto mixed lipid membranes. *J. Chem. Phys.* **2007**, *127*, 215104.
- (45) Yu, Y.; Anthony, S. M.; Zhang, L.; Bae, S. C.; Granick, S. Cationic nanoparticles stabilize zwitterionic liposomes better than anionic ones. *J. Phys. Chem. C* **2007**, *111*, 8233.
- (46) Mengistu, D. H.; Bohinc, K.; May, S. Binding of DNA to Zwitterionic Lipid Layers Mediated by Divalent Cations. *J. Phys. Chem.* B 2009, 113, 12277–12282.
- (47) Helfrich, W. Elastic Properties of Lipid Bilayers: Theory and Possible Experiments. Z. Naturforsch. 1973, 28, 693–703.
- (48) Deserno, M.; Gelbart, W. M. Adhesion and Wrapping in Colloid–Vesicle Complexes. *J. Phys. Chem. B* **2002**, *106*, 5543.

- (49) Chen, L.; Xiao, S.; Zhu, H.; Wang, L.; Liang, H. Shape-dependent internalization kinetics of nanoparticles by membranes. *Soft Matter* **2016**, *12*, 2632–2641.
- (50) Deserno, M.; Kremer, K.; Paulsen, H.; Peter, C.; Schmid, F. Computational Studies of Biomembrane Systems: Theoretical Considerations, Simulation Models, and Applications. In *From Single Molecules to Nanoscopically Structured Materials*; Basche, T., Mullen, K., Schmidt, M., Eds.; Advances in Polymer Science; Springer-Verlag Berlin: Berlin, 2014; Vol. 260, pp 237–283.
- (51) Rozycki, B.; Lipowsky, R.; Weikl, T. R. Effective surface interactions mediated by adhesive particles. *Europhys. Lett.* **2008**, *84*, 26004.
- (52) Stachowiak, J. C.; Hayden, C. C.; Sasaki, D. Y. Steric confinement of proteins on lipid membranes can drive curvature and tubulation. *Proc. Natl. Acad. Sci. U.S.A.* **2010**, *107*, 7781.
- (53) Li, S.; Malmstadt, N. Deformation and poration of lipid bilayer membranes by cationic nanoparticles. *Soft Matter* **2013**, *9*, 4969–4976.
- (54) Lipowsky, R. Spontaneous tubulation of membranes and vesicles reveals membrane tension generated by spontaneous curvature. *Faraday Discuss.* **2013**, *161*, 305–331.
- (55) Cherstvy, A. G.; Petrov, E. P. Modeling DNA condensation on freestanding cationic lipid membranes. *Phys. Chem. Chem. Phys.* **2014**, 16, 2020–2037.
- (56) Herold, C.; Schwille, P.; Petrov, E. P. Single DNA molecules on freestanding and supported cationic lipid bilayers: diverse conformational dynamics controlled by the local bilayer properties. *J. Phys. D: Appl. Phys.* **2016**, *49*, 074001.
- (57) Weikl, T. R. Indirect interactions of membrane-adsorbed cylinders. *Eur. Phys. J. E* **2003**, *12*, 265–273.
- (58) Mkrtchyan, S.; Ing, C.; Chen, J. Z. Y. Adhesion of cylindrical colloids to the surface of a membrane. *Phys. Rev. E* **2010**, *81*, 011904.
- (59) Ghosh, S. K.; Cherstvy, A. G.; Petrov, E. P.; Metzler, R. Interactions of rod-like particles on responsive elastic sheets. *Soft Matter* **2016**, *12*, 7908–7919.
- (60) Muller, M. M.; Deserno, M.; Guven, J. Balancing torques in membrane-mediated interactions: Exact results and numerical illustrations. *Phys. Rev. E* **2007**, *76*, 011921.
- (61) Kim, K. S.; Neu, J.; Oster, G. Effect of protein shape on multibody interactions between membrane inclusions. *Phys. Rev. E* **2000**, *61*, 4281–4285.
- (62) Mui, B. L.; Cullis, P. R.; Evans, E. A.; Madden, T. D. Osmotic properties of large unilamellar vesicles prepared by extrusion. *Biophys. J.* **1993**, *64*, 443–453.
- (63) Cao, R.; Kumar, D.; Dinsmore, A. D. Vesicle-Based Gel via Polyelectrolyte-Induced Adhesion: Structure, Rheology, and Response. *Langmuir* **2021**, *37*, 1714–1724.
- (64) Aimanianda, V.; Bayry, J.; Bozza, S.; Kniemeyer, O.; Perruccio, K.; Elluru, S. R.; Clavaud, C.; Paris, S.; Brakhage, A. A.; Kaveri, S. V.; Romani, L.; Latgé, J.-P. Surface hydrophobin prevents immune recognition of airborne fungal spores. *Nature* **2009**, *460*, 1117.
- (65) Raatz, M.; Lipowsky, R.; Weikl, T. R. Cooperative wrapping of nanoparticles by membrane tubes. *Soft Matter* **2014**, *10*, 3570–3577.
- (66) Yu, Y., Granick, S. Pearling of Lipid Vesicles Induced by Nanoparticles. J. Am. Chem. Soc. 2009, 131, 14158.
- (67) Gözen, I.; Billerit, C.; Dommersnes, P.; Jesorka, A.; Orwar, O. Calcium-ion-controlled nanoparticle-induced tubulation in supported flat phospholipid vesicles. *Soft Matter* **2011**, *7*, 9706–9713.
- (68) Ewers, H.; Römer, W.; Smith, A. E.; Bacia, K.; Dmitrieff, S.; Chai, W.; Mancini, R.; Kartenbeck, J.; Chambon, V.; Berland, L.; Oppenheim, A.; Schwarzmann, G.; Feizi, T.; Schwille, P.; Sens, P.; Helenius, A.; Johannes, L. GM1 structure determines SV40-induced membrane invagination and infection. *Nat. Cell Biol.* **2010**, *12*, 11–18.
- (69) Baumgart, T.; Capraro, B. R.; Zhu, C.; Das, S. L. Thermodynamics and Mechanics of Membrane Curvature Generation and Sensing by Proteins and Lipids. *Annu. Rev. Phys. Chem.* **2011**, *62*, 483–506.
- (70) Olinger, A. D.; Spangler, E. J.; Kumar, P. B. S.; Laradji, M. Membrane-mediated aggregation of anisotropically curved nanoparticles. *Faraday Discuss.* **2016**, *186*, 265–275.